# Complete and incomplete fusion in the reaction $^{35}Cl+^{12}C$ at the energy range 70–154 MeV

S. Pirrone, S. Aiello, N. Arena, Seb. Cavallaro, S. Femino', G. Lanzalone, G. Politi, F. Porto, S. Romano, and S. Sambataro
*Dipartimento di Fisica, Universitá di Catania, Universitá di Messina, Istituto Nazionale di Fisica Nucleare, Sezione di Catania, Gruppo Collegato di Messina and Laboratorio Nazionale del Sud, I-95129 Catania, Italy*
(Received 3 December 1996)

Velocity spectra of evaporation residues produced in the $^{35}Cl+^{12}C$ reaction have been measured at bombarding energies of 125, 140, and 154 MeV using time-of-flight techniques. These distributions were used to identify evaporation residues and to separate complete fusion and incomplete fusion components. The results show the presence of small contributions of incomplete fusion components which appear to be due to a cluster transfer reaction mechanism. Angular distributions and total and complete fusion evaporation residue cross sections were extracted at 70, 90, 110, 125, 140, and 154 MeV. The complete fusion cross sections and the deduced critical angular momenta are compared with other experimental data and the predictions of existing models. [S0556-2813(97)04105-8]

PACS number(s): 25.70.Jj

## I. INTRODUCTION

In previous recent works [1,2], we studied the $^{32}S$, $^{28}Si+^{12}C$ reactions around 5 MeV/nucleon in order to investigate the existence of an incomplete fusion component in the evaporation residue cross section also at this low energy. Indeed, from the kinematical analysis of the inclusive velocity spectra, we deduced that the main contribution to the evaporation residue cross sections originated from a complete fusion mechanism, but incomplete fusion components were also present. In addition, we suggested that it was possible to interpret these incomplete fusion events as generated by cluster-transfer reactions [2]. Our conclusions were in agreement with the results of other authors [3], and the values of the incomplete fusion cross sections we determined agreed with a previously established systematic [4], which correlates the fraction of incomplete fusion with the center-of-mass velocity at contact with the lighter reaction partner and with the mass asymmetry in the entrance channel.

Following the same research line, in the present paper we extend our study on the $^{35}Cl+^{12}C$ system in the energy range 70–154 MeV, also in order to reduce the lack of the experimental data in the first and second regions of the fusion excitation function because, until now, the reaction $^{35}Cl+^{12}C$ has been investigated only at the bombarding energies $E(^{35}Cl)=180$ and 200 MeV [5] and more recently at $E(^{35}Cl)=280$ MeV [6].

The experimental procedures are described in Sec. II. The experimental results and the analysis of the velocity spectra are presented in Sec. III. In Sec. IV the results of these analysis are discussed and compared to the predictions of theoretical models. Finally, the conclusions are summarized in Sec. V.

## II. EXPERIMENTAL PROCEDURE

The experiments were performed at the SPM Tandem accelerator facility of the Laboratorio Nazionale del Sud (LNS) in Catania. Self-supporting $^{12}C$ targets 40 $\mu g/cm^2$ thick were bombarded with beams of $^{35}Cl$ at 70, 90, 110, 125, 140, and 154 MeV. The targets were placed perpendicular to the beam direction.

The evaporation residues were identified in charge and mass by using a particular experimental apparatus described in detail in Ref. [7]. We remind the reader briefly that it consists of a sliding seal scattering chamber, 45 cm in diameter, which can be rotated around the target axis, and is rigidly connected to a $\Delta E$-$E$ multianode ionization chamber. A time-of-flight telescope, consisting of a microchannel-plate and a parallel-plate avalanche counter as start and stop signals detectors, respectively, is coupled to the ionization chamber. Utilizing a flight path of 118 cm an overall time resolution of 400 ps is achieved.

Typical examples of charge and mass resolution are shown in Figs. 1 and 2, respectively. The relative normalization between runs at different angles settings was established by using the elastic yields observed by two silicon surface-barrier monitor detectors placed at $\pm 9°$ with respect to the beam axis.

The absolute normalization of the differential cross sections was determined at all energies by comparing the elastic scattering data to the Rutherford scattering cross section at

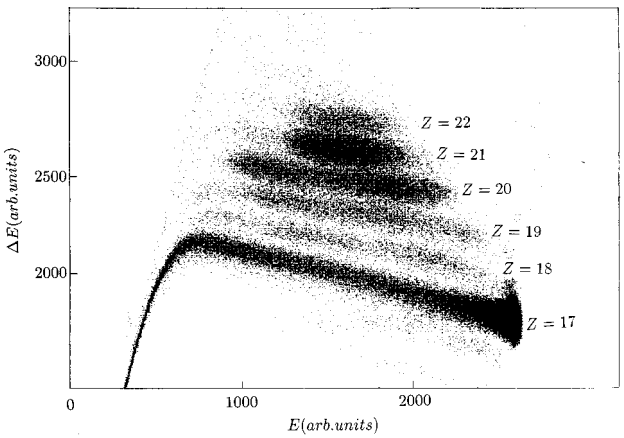


FIG. 1. Scatter plot of $\Delta E$ versus energy at 140 MeV bombarding energy and a laboratory angle of 3°.

 © 1997 The American Physical Society

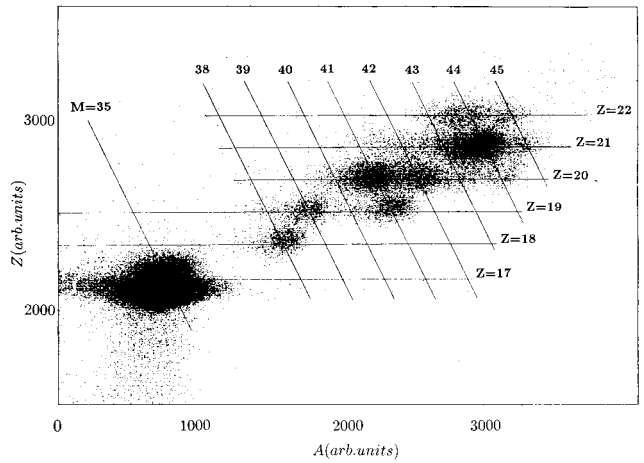


FIG. 2. Scatter plot of $Z$ versus $A$ at 140 MeV bombarding energy and a laboratory angle of 3°.

very forward angles. The systematic uncertainty in this normalization procedure has been estimated to be less than 5%.

## III. EXPERIMENTAL RESULTS AND ANALYSIS

### A. Elastic scattering

The elastic scattering angular distributions were measured over the angular range $2.5° \leqslant \vartheta_L \leqslant 12°$, in steps ranging from 0.5° at small angles to 2° at the larger ones.

In Fig. 3 the experimental ratios $\sigma_{\rm el}/\sigma_{\rm Ruth}$ between the elastic and Rutherford cross sections at energies $E(^{35}\mathrm{Cl}) = 70$, 90, 110, 125, 140, and 154 MeV versus the laboratory angle are reported. The solid lines in the same figure correspond to optical model fits obtained by using the code PTOLEMY [8] with the parameters of Table I. In the same table the total reaction cross sections $\sigma_r$(OM) obtained by means of the optical model analysis are reported.

### B. Velocity spectra

At the three highest energies $E(^{35}\mathrm{Cl}) = 125$, 140, and 154 MeV, the velocity spectrum for each residue mass ($38 \leqslant A \leqslant 44$) was decomposed with a Gaussian fitting procedure [1,2,9–11] to determine the complete fusion contribution. For the lower energies $E(^{35}\mathrm{Cl}) = 70$, 90, and 110 MeV, no attempt was made to separate the evaporation residue cross sections into complete fusion and incomplete fusion components, because, as is well known at these energies, the total reaction cross sections, in practice, coincide with the complete fusion cross sections.

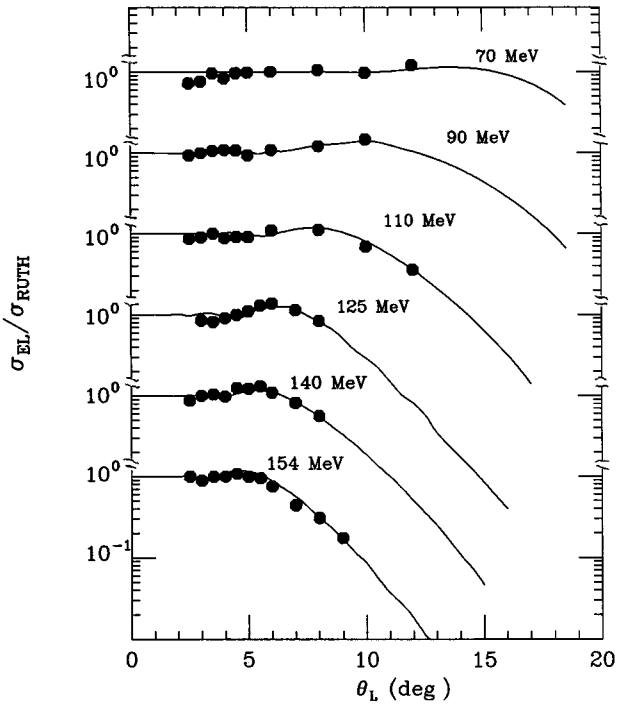


FIG. 3. Elastic scattering cross section normalized to Rutherford scattering. The solid lines are the results of optical model fits.

Figures 4, 5, and 6 exhibit typical velocity spectra of separated individual masses at $\vartheta_L = 3°$ and $E(^{35}\mathrm{Cl}) = 125$, 140, and 154 MeV, respectively. The shape of the velocity spectra was found to be consistent with the assumption that the main contribution arises from the evaporation residue following complete fusion. In fact, in the Galilean-invariant representation $1/V^2 \cdot d^2\sigma/dV\, d\Omega$, the structures are symmetrical with respect to the compound nucleus velocity [9]. The position and width of the complete fusion component further confirm the previous considerations. In Fig. 7 are reported for each evaporation residue, at $E(^{35}\mathrm{Cl}) = 125$, 140, and 154 MeV, the ratios of velocity centroids $\underline{V}_{\rm CN}\cos\vartheta_L$, expected in the case of complete fusion, to the $V_R$ ones obtained by fitting the experimental velocity spectra with standard formula [9,11].

Figure 8 shows the ratios of the standard deviation $s$ of the velocity distributions, obtained by means of the fit procedure, to the ones expected in the case of complete fusion $s_{\rm CF}$ [11]. In the $s_{\rm CF}$ formula the value $a = A/10$ was assumed for the level density parameter.

TABLE I. Elastic scattering optical model fit parameters and total reaction cross sections derived from the fits. Only the well depth $V_R$ and $V_I$ were allowed to vary during the fit.

| $E_{\rm lab}$ (MeV) | $V_R$ (MeV) | $V_I$ (MeV) | $r_{0R}$ (fm) | $r_{0I}$ (fm) | $a_R$ (fm) | $a_I$ (fm) | $\sigma_r$(OM) (mb) |
|---|---|---|---|---|---|---|---|
| 70 | 3.05 | 2.38 | 1.30 | 1.16 | 0.62 | 0.61 | 329 |
| 90 | 14.9 | 2.10 | 1.30 | 1.16 | 0.62 | 0.61 | 686 |
| 110 | 8.87 | 14.9 | 1.30 | 1.16 | 0.62 | 0.61 | 969 |
| 125 | 12.7 | 11.0 | 1.30 | 1.16 | 0.62 | 0.61 | 1115 |
| 140 | 8.9 | 19.9 | 1.30 | 1.16 | 0.62 | 0.61 | 1260 |
| 154 | 11.7 | 25.8 | 1.30 | 1.16 | 0.62 | 0.61 | 1417 |

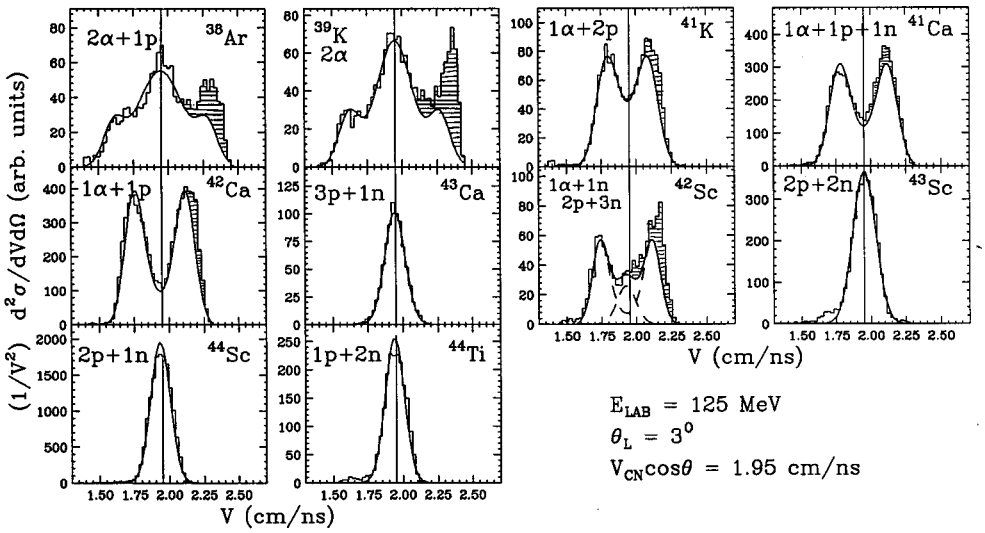


FIG. 4. Invariant velocity spectra of evaporation residues at $E(^{35}\mathrm{Cl})=125$ MeV and $\vartheta_L=3°$. The curves centered at $V_{\mathrm{CN}}\cos\vartheta_L$ (vertical line) represent the contributions of complete fusion followed by evaporation of nucleon ($xN$) and $\alpha$ particles plus nucleon ($y\alpha+xN$). The histograms are the experimental data. The hatched areas originate from cluster transfer reactions.

In both graphics the experimental values agree, within the errors, with the theoretical expectations.

For some masses ($A=38,39,41,42$), we observe further structures (hatched areas in Figs. 4, 5, and 6) which cannot be explained as due to complete fusion. The velocities corresponding to these structures are larger than the velocity centroid $V_{\mathrm{CN}}\cos\vartheta_L$ expected in the case of compound nucleus so that, since we studied the system in reverse kinematic, we expect that these structures originated from incomplete fusion [4].

Particularly, we interpreted the hatched areas as a cross section due to an incomplete fusion reaction governed by a cluster transfer reaction mechanism: the $^{41}$K, $^{41}$Ca, $^{42}$Ca, and $^{42}$Sc masses originating from $^{8}$Be transfer ($^{35}\mathrm{Cl}+^{12}\mathrm{C}\rightarrow{}^{43}\mathrm{Sc}^{*}+\alpha$; $^{43}\mathrm{Sc}^{*}\rightarrow{}^{41}\mathrm{K}+2p$, $^{41}\mathrm{Ca}+1n+1p$, $^{42}\mathrm{Ca}+1p$, $^{42}\mathrm{Sc}+1n$, respectively) and the $^{39}$K and $^{38}$Ar masses from $\alpha$ transfer ($^{35}\mathrm{Cl}+^{12}\mathrm{C}\rightarrow{}^{39}\mathrm{K}^{*}+{}^{8}\mathrm{Be}$; $^{39}\mathrm{K}^{*}\rightarrow{}^{39}\mathrm{K}+\gamma$ and $^{39}\mathrm{K}^{*}\rightarrow{}^{38}\mathrm{Ar}+1p$).

We draw these conclusions by comparing the implications derived from simple reaction models proposed for incomplete fusion, i.e., breakup fusion (BUF) and massive transfer (MT).

We recall that assuming the BUF mechanism [12,13], the $^{12}$C must break into an $\alpha$ particle and a $^{8}$Be in the first stage of the reaction and, successively, one of these fragments fuses with the projectile while the other fragment continues to move with almost the same velocity in the c.m. system. Refering to the laboratory energy $E(^{35}\mathrm{Cl})=154$ MeV, an incomplete fusion reaction with an $\alpha$ particle, e.g., $^{35}\mathrm{Cl}+\alpha$, leads to an excitation energy $E^{*}(^{39}\mathrm{K})=\frac{4}{39}E(^{35}\mathrm{Cl})+Q_{gg}(-0.148\ \mathrm{MeV})\approx16$ MeV. Similarly, the $^{35}\mathrm{Cl}+{}^{8}\mathrm{Be}$ reaction leads to an excitation energy $E^{*}(^{43}\mathrm{Sc})=\frac{8}{43}E(^{35}\mathrm{Cl})+Q_{gg}(4.75\ \mathrm{MeV})\approx33$ MeV.

In the picture of the MT model [14–16], the production of a given residual nucleus can be considered as the result of a two-step process. First, a nucleon or a group of nucleons is transferred from the projectile to the target. Second, this intermediate nucleus dissipates its excitation energy by evaporating neutrons or emitting photons. These massive transfer reactions, as is known, form a class of reactions which form a bridge between the complete fusion processes and deep inelastic and direct processes.

The reaction is characterized by a ''$Q$ value window'' centered at so-called ''$Q$ optimum.'' In this case the excitation energy is calculated as $E^{*}=Q_{gg}-Q_{\mathrm{opt}}$, where $Q_{\mathrm{opt}}=(Z_3Z_4/Z_1Z_2-1)E^{i}_{\mathrm{c.m.}}$, in which the indices 1,2 and 3,4 indicate the entrance ($i$) and the exit channel, respectively [17,18]. By using the previous formulas, we found the excitation energies $E^{*}(^{43}\mathrm{Sc})\approx28$ MeV, for a $^{8}$Be transfer, and

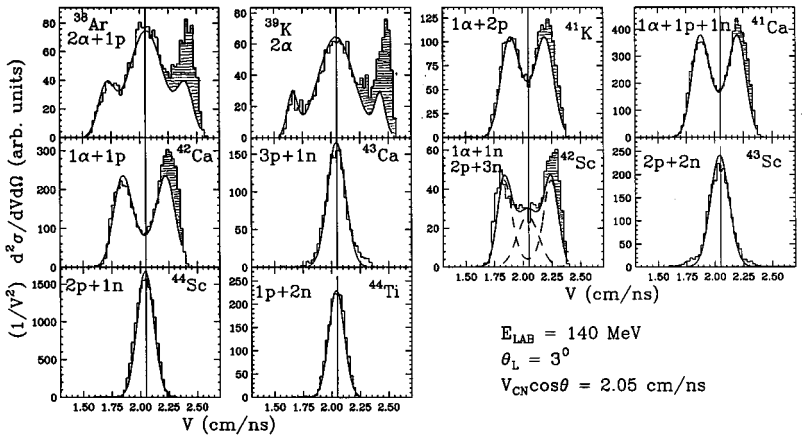


FIG. 5. Same as Fig. 4 at $E(^{35}\mathrm{Cl})=140$ MeV and $\vartheta_L=3°$.

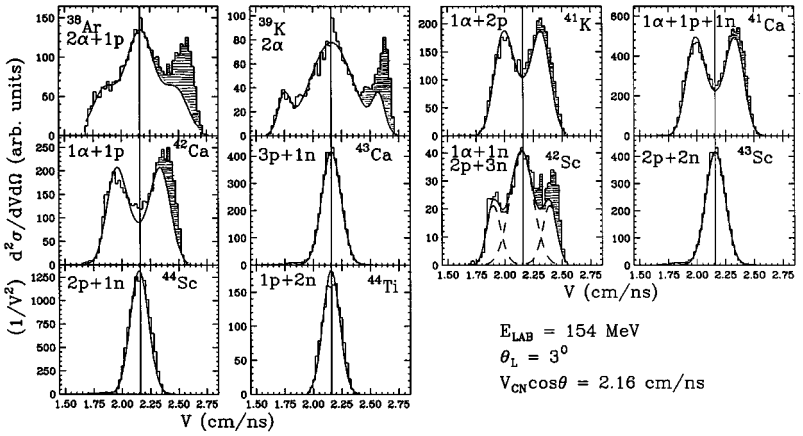


FIG. 6. Same as Fig. 4 at $E(^{35}\mathrm{Cl})=154$ MeV and $\vartheta_L=3°$.

$E^*(^{39}\mathrm{K})\approx 10$ MeV, for an $\alpha$ transfer.

For the incomplete fusion contributions originating from $^{43}$Sc* ($^{42}$Sc, $^{42}$Ca, $^{41}$Ca, $^{39}$K residues), the above excitation energies $E(^{43}\mathrm{Sc}^*)\approx 33$ and 28 MeV, calculated, respectively, in the BUF and MT frameworks, are enough for $1N$, $2N$, or $1\alpha$-particle evaporation. In fact, in this mass region, the mean excitation energy removed by a nucleon or an $\alpha$-particle evaporation is about 16 and 22 MeV, respectively [10]. Therefore the excitation energies are not able to discriminate between the two mechanisms.

As regards the incomplete fusion contributions originating from $^{39}$K* ($^{39}$K, $^{38}$Ar residues), the BUF excitation energy $E(^{39}\mathrm{K}^*)\approx 16$ MeV is enough for a single nucleon evaporation so that we should detect only the $^{38}$Ar nuclide produced in the reaction ($^{35}\mathrm{Cl}+^{12}\mathrm{C}\rightarrow{}^{39}\mathrm{K}^*+{}^{8}\mathrm{Be}$; $^{39}\mathrm{K}^*\rightarrow{}^{38}\mathrm{Ar}+1p$) and not the $^{39}$K nuclide which indeed we observed experimentally. This last result is confirmed by the calculation performed with the code CASCADE [19], which predicts the possibility of $1p$ decay only. So that, in the BUF framework, we cannot justify the presence of the $^{39}$K nuclide, experimentally observed.

On the other hand, the MT excitation energy $E(^{39}\mathrm{K}^*)\approx 10$ MeV, and this value, in principle, does not allow nucleon evaporation, so that we cannot justify the $^{38}$Ar nuclide contribution, even if in this case the CASCADE calculations predict the possibility of gamma and $1p$ decays.

Therefore, from the previous considerations we can conclude that, in our case, the excitation energies, calculated in the BUF and MT models, are not a discriminant argument to distinguish between the two mechanism of the incomplete fusion.

As a consequence, the observation of the trend of the incomplete fusion residue velocities constitutes a good probe to discriminate among the various reaction mechanism. In Fig. 9 we report the ratios between the experimental velocity

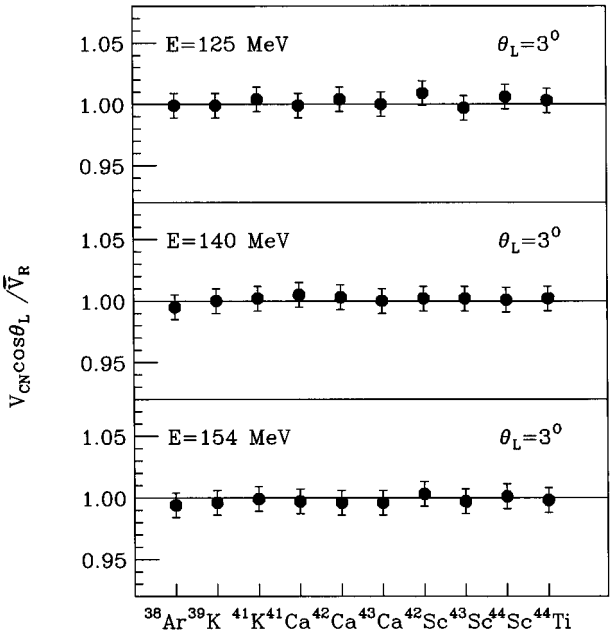


FIG. 7. Ratio of velocity centroids expected in the case of complete fusion to those obtained by fitting the experimental velocity spectra, plotted for different evaporation residues.

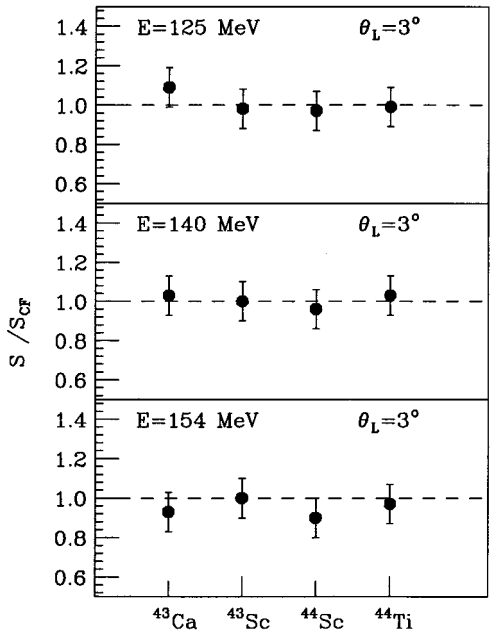


FIG. 8. Ratio of measured standard deviation ($s$) obtained by fitting the velocity spectra of residues produced with nucleon evaporation to the values expected in the case of complete fusion ($s_{\mathrm{CF}}$).

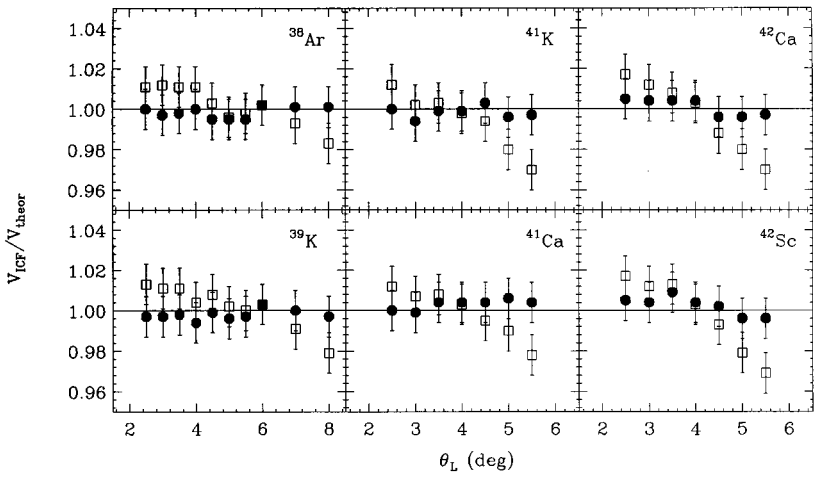


FIG. 9. Ratio of the experimental velocities of the incomplete fusion contributions $V_{ICF}$ to those expected in the case of break up fusion (open squares) and cluster transfer (solid circles), plotted versus laboratory angle at $E(^{35}\mathrm{Cl}) = 154$ MeV.

values of the incomplete fusion component and those calculated assuming a breakup fusion (open squares) or a massive transfer (solid circles) mechanism, respectively, at various angles and at 154 MeV energy. For all masses, the ratios calculated in the MT frame are equal to 1, within the experimental errors, while the trends of ratios obtained in the BUF frame show at small angles values larger than 1 and at larger angles values smaller than 1. We note that similar results are obtained for the other bombarding energies $E(^{35}\mathrm{Cl}) = 125$ and 140 MeV also.

A further argument which confirms the hypothesis that the incomplete fusion components originate from cluster transfer reaction can be derived from the slope of the angular distributions, as we will show in the next subsection.

### C. Angular distributions

Figure 10 shows the differential angular distributions of the residues formed by complete and incomplete fusion for the $^{35}\mathrm{Cl}+^{12}\mathrm{C}$ reaction at 140 MeV. The exponential slope of the angular distributions of incomplete fusion products (lower part of the figure) differs markedly from complete fusion (upper part of the figure), thus indicating a reaction mechanism different from fusion. Particularly, this mechanism seems to be attributed to a massive transfer reaction, because, as is well known, the breakup fusion mechanism shows fusionlike angular distributions.

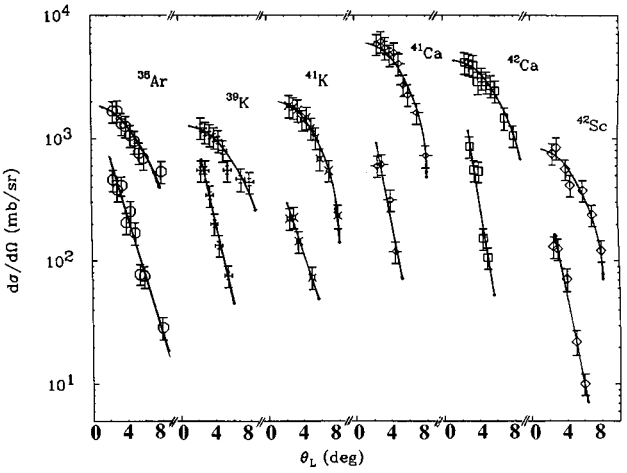


FIG. 10. Angular distributions of evaporation residues from complete fusion (upper part) and incomplete fusion (lower part). The solid lines are drawn only as a guide for the eye.

The angular distributions at 125 and 154 MeV energies show the same trend.

By integrating the angular distributions, we obtain the absolute cross sections for complete and incomplete fusion. Partial and total cross sections are listed in Table II for $E(^{35}\mathrm{Cl}) = 125$, 140, and 154 MeV. We point out that the possible contribution of the evaporation residue $^{35}$Cl to the complete fusion cross section has not been experimentally determined because of the intense background present in the $^{35}$Cl spectra. The values predicted by code LILITA [20] for the cross section of this residue at the various energies are reported in the same Table II.

## IV. COMPARISON WITH THEORY AND DISCUSSION

The experimental fusion angular distributions for each atomic number ($18 \leqslant Z \leqslant 22$) detected at $E(^{35}\mathrm{Cl}) = 70$, 90, 110, 125, 140, and 154 MeV are shown in Fig. 11 together with the statistical model calculations (open histograms) obtained by using the Monte Carlo code LILITA. We used as input data for the code LILITA the measured total fusion cross sections as reported in Table III and the value $a = A/10$ for the level density parameter. The spin cutoff parameter is calculated assuming a radius $r_0 = 1.2$ fm. In general, there is a satisfactory agreement for all the considered energies.

Similar good comparisons between experimental and calculated relative mass and charge yields are shown in Fig. 12.

In Fig. 13 we display the experimental fusion cross sections available to date on the $^{35}\mathrm{Cl}+^{12}\mathrm{C}$ system as a function of $E_{\mathrm{c.m.}}^{-1}$. There, the solid circles are the present results, while the open circles are taken from Beck *et al.* [5,6].

In the same figure we report the predictions of the Matsuse *et al.* [21] and the Bass [22] models as dashed and solid curves, respectively.

In the framework of the critical distance model of Matsuse *et al.* [21], the fusion cross section is evaluated in the three different energy regions by means of the following expressions:

TABLE II. Values of the complete ($\sigma_{CF}$) and incomplete ($\sigma_{ICF}$) fusion cross sections for each evaporation residue at $E(^{35}Cl) = 125$, 140, and 154 MeV. The reported value for $^{35}Cl^a$ represents the cross section predicted by the evaporation code LILITA for this residue. In the last line we report the total fusion cross section obtained considering the measured and calculated cross sections.

| | $E = 125$ MeV | | $E = 140$ MeV | | $E = 154$ MeV | |
|---|---|---|---|---|---|---|
| | $\sigma_{CF}$ (mb) | $\sigma_{ICF}$ (mb) | $\sigma_{CF}$ (mb) | $\sigma_{ICF}$ (mb) | $\sigma_{CF}$ (mb) | $\sigma_{ICF}$ (mb) |
| $^{37}Ar$ | 4±1 | | 5±1 | | 16±2 | |
| $^{38}Ar$ | 45±10 | 6±2 | 55±11 | 10±2 | 97±20 | 19±4 |
| $^{38}K$ | 6±1 | | 7±1 | | 17±2 | |
| $^{39}K$ | 56±11 | 6±2 | 36±7 | 10±2 | 55±11 | 11±2 |
| $^{40}K$ | 12±1 | | 16±2 | | 40±4 | |
| $^{41}K$ | 37±8 | 1±.5 | 66±13 | 5±1 | 79±16 | 4±1 |
| $^{40}Ca$ | 23±2 | | 21±2 | | 27±3 | |
| $^{41}Ca$ | 165±33 | 14±3 | 204±40 | 8±2 | 222±44 | 11±2 |
| $^{42}Ca$ | 210±42 | 2±1 | 172±34 | 13±3 | 109±21 | 11±2 |
| $^{43}Ca$ | 18±3 | | 24±2 | | 41±4 | |
| $^{44}Ca$ | 13±1 | | 17±2 | | 14±1 | |
| $^{42}Sc$ | 34±7 | 2±1 | 29±6 | 3±1 | 22±2 | 4±1 |
| $^{43}Sc$ | 45±5 | | 44±4 | | 58±6 | |
| $^{44}Sc$ | 167±17 | | 232±23 | | 169±17 | |
| $^{45}Sc$ | 56±6 | | 24±2 | | 25±2 | |
| $^{43}Ti$ | 5±1 | | | | | |
| $^{44}Ti$ | 25±3 | | 26±3 | | 21±2 | |
| $^{45}Ti$ | 43±4 | | 29±3 | | 12±1 | |
| $^{46}Ti$ | 7±1 | | | | | |
| $\Sigma\sigma$ | 970±160 | 31±10 | 1007±156 | 59±11 | 1024±155 | 60±12 |
| $^{35}Cl^a$ | 0 | | 6 | | 12 | |
| $\Sigma\sigma + \sigma(^{35}Cl)$ | 970±160 | | 1013±156 | | 1036±155 | |

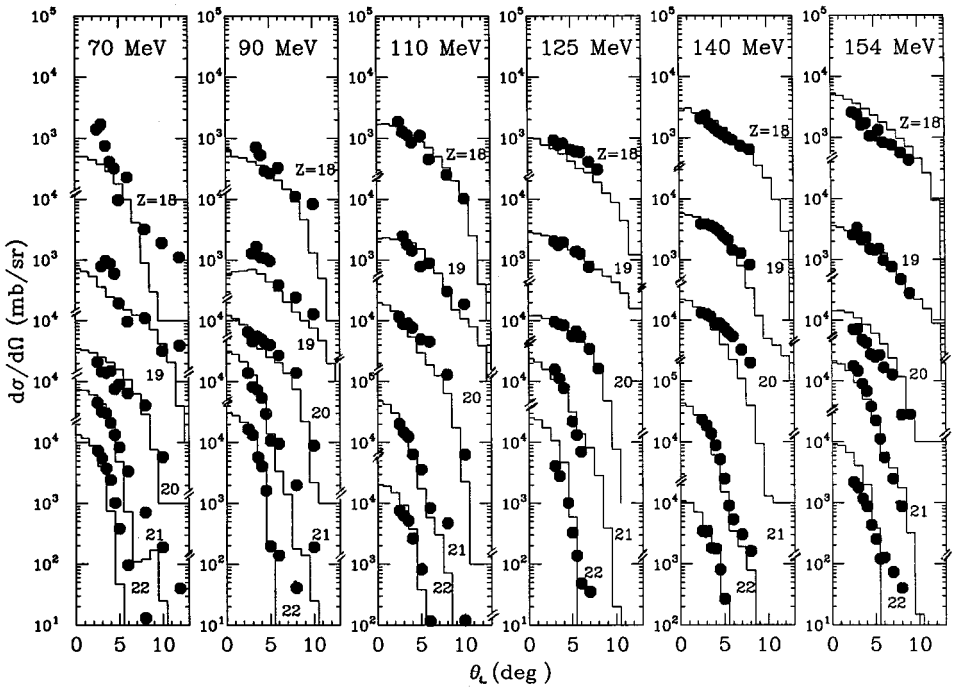


FIG. 11. Comparison of experimental angular distribution of the complete fusion (closed circles) with the prediction of evaporation LILITA code (histograms) for each $Z > 17$ detected at $E(^{35}Cl) = 70$, 90, 110, 125, 140, and 154 MeV.

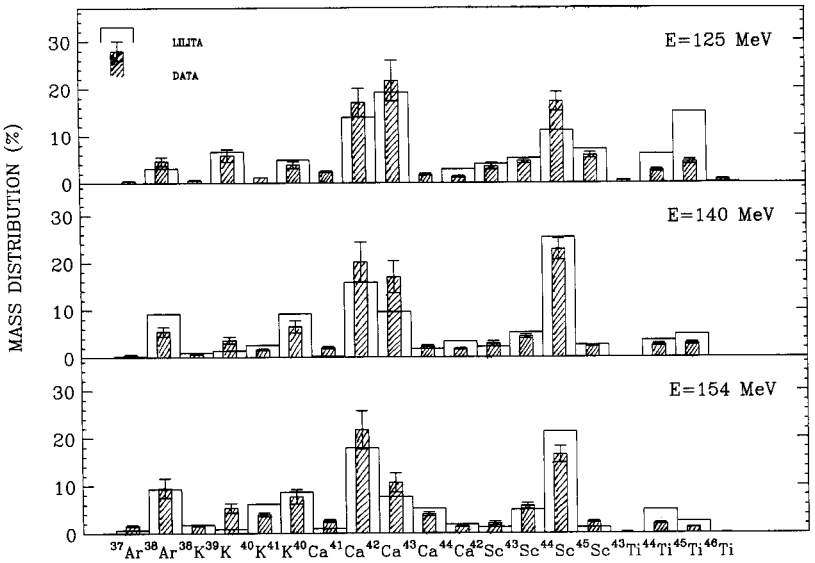


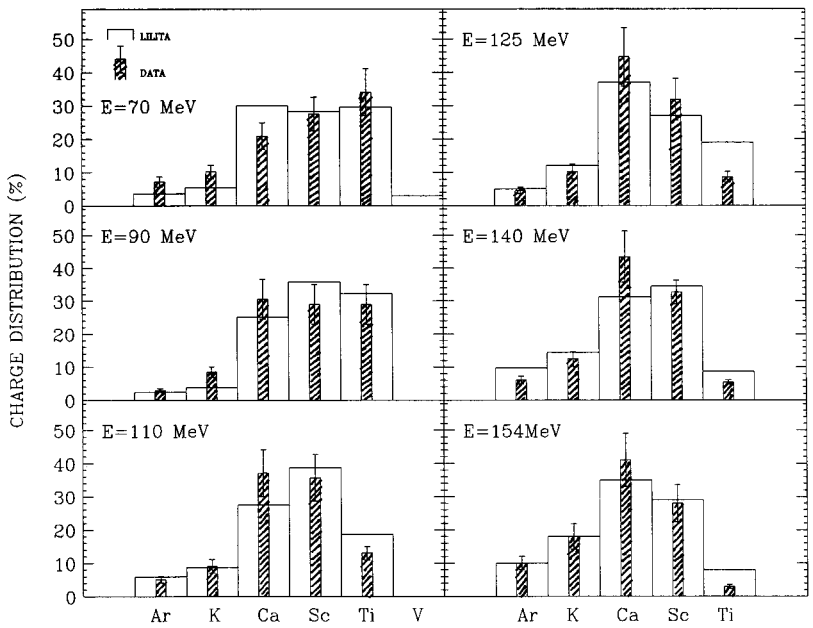


FIG. 12. Upper part: experimental relative mass yields of the fusion residues (hatched bars) compared with LILITA calculations (open histograms) for $E(^{35}\mathrm{Cl})=110$, 125, and 140. Lower part: same as upper part for charge and for all studied energies.

region I (low energy region) $\sigma_{\mathrm{CF}}^{\mathrm{I}}=\pi R_B^2\left(1-\dfrac{V_B(R_B)}{E_{\mathrm{c.m.}}}\right)$,

region II (central energy region) $\sigma_{\mathrm{CF}}^{\mathrm{II}}=\left(\dfrac{\pi I}{\mu}\right)\left[1+\dfrac{Q-\Delta Q}{E_{\mathrm{c.m.}}}\right]$,

region III (high energy region)

$$\sigma_{\mathrm{CF}}^{\mathrm{III}}=\pi\langle d^2\rangle\left(1+\frac{[\frac{1}{2}\mu\omega_d^2\langle d^2\rangle-U_C[(\langle d^2\rangle)^{1/2}]+Q]}{E_{\mathrm{c.m.}}}\right),$$

where $(\langle d^2\rangle)^{1/2}$ is the critical distance between the colliding nuclei.

In the present calculations, the following parameters have been used: For $\sigma_{\mathrm{CF}}^{\mathrm{I}}$, $V_B(R_B)=V_C(R_C)=Z_1Z_2e^2/R_C$, $R_C=R_0+\Delta R_C$, and $R_B=R_0+\Delta R_B$, with $R_0=R_1+R_2$, $R_i=1.12A_i^{1/3}-0.86A_i^{-1/3}$, $\Delta R_B=3.05$ fm, and $\Delta R_C=3.70$ fm. For $\sigma_{\mathrm{CF}}^{\mathrm{II}}$, $I=2/3AM\langle r^2\rangle_A\alpha$, where $M$ is the nucleon mass, $\langle r^2\rangle_A=\frac{3}{5}(1.12A^{1/3})^2(1+3.84A^{-2/3})$, $\alpha=0.80$, and $\Delta Q=13$ MeV. For $\sigma_{\mathrm{CF}}^{\mathrm{III}}$, $\omega_d=\beta\omega$, with $\omega=40A^{-1/3}/\hbar$ and $\beta=0.72$.

The theoretical prediction of the Bass model is obtained by using the following empirical nuclear potential:

$$V_n(s)=\frac{R_1R_2}{R_1+R_2}\,g(s),$$

where

$$g(s)=[A\,\exp(s/d_1)+B\,\exp(s/d_2)]^{-1}.$$

The parameters used in the calculations are those reported in Ref. [22], based on a global fit to fusion data, i.e., $A$

TABLE III. Complete fusion cross sections ($\sigma_{CF}$) and critical angular momenta ($l_{cr}$) for all studied energies.

| $E_{lab}$ (MeV) | $E_{c.m.}$ (MeV) | $\sigma_{CF}$ (mb) | $l_{cr}$ ($\hbar$) |
|---|---|---|---|
| 70 | 17.9 | 302±60 | 8.1±0.8 |
| 90 | 23.0 | 770±125 | 15.0±1.2 |
| 110 | 28.1 | 990±150 | 18.9±1.4 |
| 125 | 31.9 | 970±160 | 20.0±1.6 |
| 140 | 35.7 | 1013±156 | 21.7±1.6 |
| 154 | 39.3 | 1036±155 | 23.0±1.7 |

$=0.03$ MeV$^{-1}$ fm, $B=0.006$ MeV$^{-1}$, $d_1=3.30$ fm, $d_2=0.65$ fm, and $R_i=1.16A_i^{1/3}-1.39A_i^{-1/3}$.

Both calculations reproduce the experimental data quite well in the first and second energy regions so that the discrimination between the two models depends essentially on the experimental points in the third energy region. In this region, at present, there is only the experimental data at $E(^{35}\mathrm{Cl})=280$ MeV, which is better fitted by the Matsuse curve. However, a more convincing argument in favor of this last model should be derived only from the knowledge of other new experimental data at the highest energy.

The critical angular momenta, extracted from the complete fusion cross sections using the sharp cutoff approximation, are listed in Table III, where the uncertainty in the $l_{cr}$ represents the experimental uncertainty in the cross section.

A plot of excitation energy as a function of the $l_{cr}$ for fusion is shown in Fig. 14, for the present data and for data extracted from previous results [5,6,10,23], relative to different entrance channels that populate the same compound nucleus $^{47}$V.

The solid line showed in the figure is the statistical yrast line [24], calculated with $r_0=1.2$ fm and $\Delta Q=10$ MeV. With the exception of the data of Beck *et al.* [6] at $E^*(^{47}\mathrm{V})=88$ MeV, the behavior of all analyzed systems in the intermediate excitation energy range [30 MeV $<E^*(^{47}\mathrm{V})<90$ MeV] is reproduced rather well by this line. The data of the $^{20}$Ne+$^{27}$Al system [10] show a saturation value in the critical angular momentum which agrees with the calculated Sierk fission barrier limit [25,26] of the $^{47}$V compound nucleus, represented by the vertical dashed line in the figure. The $l_{cr}=27.5\hbar$ value reported in Ref. [6] might indicate the existence of a limitation on high energy cross section imposed by the entrance channel. We observe, besides, that this $l_{cr}$ value, extracted from the evaporation residue cross section, should be lower, taking into account a contribution of about 20% of the incomplete fusion components in the evaporation residue cross section as predicted by the systematics of Morgenstern *et al.* [4].

## V. CONCLUSIONS

In this paper we have presented the elastic scattering cross sections and the mass, charge, and angular distributions for the evaporation residues produced in the reaction $^{35}$Cl+$^{12}$C in the energy range $E(^{35}\mathrm{Cl})=70-154$ MeV.

From the analysis of the velocity spectra, performed at the three highest energies $E(^{35}\mathrm{Cl})=125$, 140, and 154 MeV, we deduced that the main contributions to the evaporation residue cross sections originate from a complete fusion mechanism, but for all energies incomplete fusion components are also present. We interpret these incomplete fusion events, as generated by cluster transfer reactions. This last result is in agreement with the ones obtained analysing the $^{28}$Si+$^{12}$C at bombarding energies ranging from 3.7 and 5.5 MeV/nucleon. Values of the incomplete fusion cross sections of about 3–6 % of the deduced complete fusion cross sections are in agreement with a previously established systematics [4], which correlates the fraction of incomplete fusion with the center-of-mass velocity at contact with the lighter reaction partner and with the mass asymmetry in the entrance channel.

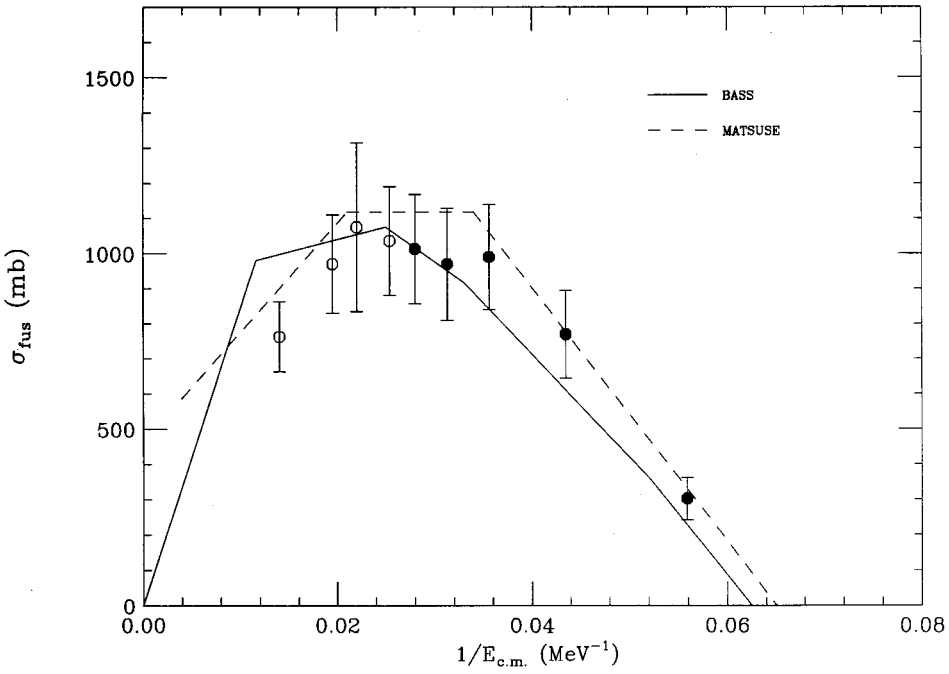


FIG. 13. Complete fusion evaporation residue cross section as a function of $E_{c.m.}^{-1}$. The solid circles are the present data, and the open circles are the data reported from Beck *et al.* [5,6]. The dashed and solid curves are the results of fusion model calculations of Refs. [21] and [22], respectively.

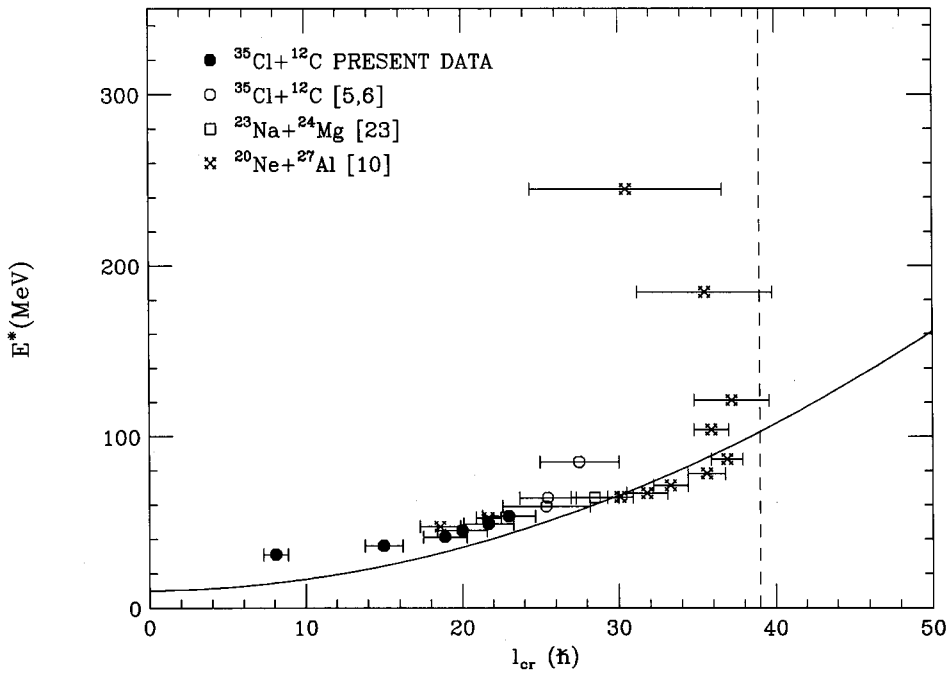


FIG. 14. Critical angular momenta for different complete fusion reactions leading to the $^{47}$V compound nucleus at different excitation energies. The solid curve corresponds to the statistical yrast line [24] calculated with $r_0 = 1.2$ fm and $\Delta Q = 10$ MeV. The dashed line indicates the angular momentum at which the fission barrier vanishes as predicted by the Sierk model [25,26].

The experimental excitation function constructed by present data and those available at present in the literature is quite in agreement especially in the first and second energy regions with the theoretical previsions derived in the frame of the Bass and Matsuse models.

Finally, the critical angular momenta extracted from the complete fusion evaporation residue cross sections show a saturation at high energies which is consistent with the calculated Sierk fission barrier [25,26] limit of the $^{47}$V compound nucleus. The value $l_{cr} = 27.5\hbar$ at $E^*(^{47}\mathrm{V}) = 88$ MeV, deduced recently from Beck *et al.*, could indicate a saturation in the critical angular momentum at a different lower value and consequently the existence of a limitation on the fusion cross section imposed by the entrance channel.

Since the $l_{cr}$ values deduced from our experimental data are confined in the $30\ \mathrm{MeV} < E^*(^{47}\mathrm{V}) < 55\ \mathrm{MeV}$ excitation energy range, we cannot rule out the possibility of an entrance channel limitation in the complete fusion cross sections.

Additional measurements for systems leading to $^{47}$V compound nucleus at high excitation energies [$E^*(^{47}\mathrm{V}) > 90$ MeV] are required to determine whether the observed differences in the values of the critical angular momentum really reflect an entrance channel dependence.

## ACKNOWLEDGMENTS

We would like to thank the Laboratorio Nazionale del Sud (Catania) accelerator staff for their assistance in providing the beam in the experiment. Besides, thanks are due to V. Campagna for technical help during the measurements.

[1] N. Arena, Seb. Cavallaro, S. Feminó, P. Figuera, S. Pirrone, F. Porto, and S. Sambataro, Phys. Rev. C **44**, 1947 (1991).

[2] N. Arena, Seb. Cavallaro, S. Feminó, P. Figuera, S. Pirrone, G. Politi, F. Porto, S. Romano, and S. Sambataro, Phys. Rev. C **50**, 880 (1994).

[3] H. Morgenstern, W. Bohne, W. Golster, and K. Grabish, Z. Phys. A **324**, 443 (1986).

[4] H. Morgenstern, W. Bohne, W. Golster, K. Grabisch, and A. Kyenowski, Phys. Rev. Lett. **52**, 1104 (1984).

[5] C. Beck, B. Djerroud, F. Haas, R. M. Freeman, A. Hachem, B. Heusch, A. Morsad, M. Youlal, Y. Abe, A. Dayras, J. P. Wieleczko, B. T. Matsuse, and S. M. Lee, Z. Phys. A **343**, 309 (1992).

[6] C. Beck, D. Mahboub, R. Nouicer, T. Matsuse, B. Djerroud, R. M. Freeman, F. Haas, A. Hachem, A. Morsad, M. Youlel, S. J. Sanders, R. Dayras, J. P. Wieleczko, E. Berthoumieux, R. Legrain, E. Pollacco, Sl. Cavallaro, E. De Filippo, G. Lanzanó, A. Pagano, and M. L. Sperduto, Phys. Rev. C **54**, 227 (1996).

[7] P. Figuera, S. Pirrone, A. Anzalone, N. Arena, Seb. Cavallaro, S. Femino', F. Giustolisi, F. Porto, and S. Sambataro, Nuovo Cimento A **104**, 251 (1991).

[8] M. H. Farlane and S. C. Poeper, Argonne National Laboratory Report No. ANL-76-11, 1978.

[9] J. Gomez del Campo, R. G. Stokstad, J. A. Biggerstaff, R. A. Dayras, A. H. Snell, and P. H. Stelson, Phys. Rev. C **19**, 2170 (1979).

[10] H. Morgenstern, W. Bohne, W. Grabish, H. Lehr, and W. Stoffler, Z. Phys. A **313**, 39 (1983).

[11] W. Galster, H. Morgenstern, W. Bohne, K. Grabish, and A. Kyanowski, in *Proceedings of the Tsukuba International Symposium*, edited by K. Furuno and T. Kishimoto (World Scientific, Singapore, 1984), p. 248.

[12] T. Udagawa and T. Tamura, Phys. Rev. Lett. **45**, 1311 (1980).
[13] E. Takada, T. Shimoda, N. Takahashi, T. Yamaya, K. Nagatani, T. Udagawa, and T. Tamura, Phys. Rev. C **23**, 722 (1981).
[14] D. R. Zolnowski, H. Yamada, S. E. Cala, A. C. Kahler, and T. T. Sugihara, Phys. Rev. Lett. **41**, 92 (1978).
[15] H. Yamada, D. R. Zolnowski, S. E. Cala, A. C. Kahler, J. Pierce, and T. T. Sugihara, Phys. Rev. Lett. **43**, 605 (1979).
[16] R. Bimbot, D. Gardes, and M. F. Rivet, Nucl. Phys. **A189**, 193 (1972).
[17] Ch. Toepffer, Z. Phys. **253**, 78 (1972).
[18] P. J. A. Buttle and L. J. B. Goldfarb, Nucl. Phys. **A176**, 299 (1971).
[19] F. Pühlhofer, Nucl. Phys. **A280**, 267 (1977).
[20] J. Gomez del Campo and R. G. Stokstad, ''LILITA, a Monte Carlo Statistical Model Code,'' Oak Ridge National Laboratory Technical Memo No. ORNL-TM-7295, 1981 (unpublished).
[21] T. Matsuse, A. Arima, and S. M. Lee, Phys. Rev. C **26**, 2338 (1982).
[22] R. Bass, Phys. Rev. Lett. **39**, 265 (1977).
[23] C. Beck, B. Djerroud, F. Haas, R. M. Freeman, A. Hachem, B. Heusch, A. Morsad, M. Vuillet-A-Cilles, and S. J. Sanders, Phys. Rev. C **47**, 2093 (1993).
[24] S. M. Lee, T. Matsuse, and A. Arima, Phys. Rev. Lett. **45**, 165 (1980).
[25] Arnold J. Sierk, Phys. Rev. C **33**, 2039 (1986).
[26] S. J. Sanders, Phys. Rev. C **44**, 2676 (1991).